Non-degenerate-pump four-wave mixing kinetic inductance travelling-wave parametric amplifiers

Engineering Research Express

OPEN ACCESS

RECEIVED
13 November 2023

REVISED
11 January 2024

ACCEPTED FOR PUBLICATION
22 January 2024

PUBLISHED
1 February 2024

PAPER

Non-degenerate-pump four-wave mixing kinetic inductance travelling-wave parametric amplifiers

J C Longden and B-K Tan

Department of Physics (Astrophysics), University of Oxford, Denys Wilkinson Building, Keble Road, Oxford, OX1 3RH, United Kingdom

E-mail: joseph.longden@physics.ox.ac.uk **and** boonkok.tan@physics.ox.ac.uk

Keywords: parametric amplifier, travelling-wave, kinetic inductance, Superconducting thin films, wave mixing

Abstract

Kinetic inductance travelling-wave parametric amplifiers (KITWPAs) have been demonstrated to achieve high gain over broad bandwidths whilst achieving near quantum-limited noise performance, properties which are extremely important for many ultra-sensitive experiments. In early KITWPA designs, the requirement for phase-matching lead to the creation of a large zero-gain gap in the centre of the gain profile where the peak gain is, which also slightly narrows down the operational bandwidth of the device. This has been mitigated in more recent designs by introducing a DC bias to the KITWPA device, which allows the gap to be tuned away from the amplification band. However, the added DC biasing requires a more complicated experimental setup and potentially leads to unwanted heat leak in the cryogenic environment. Additionally, operation with a DC bias also become challenging at higher frequencies beyond the microwave regime. In this paper, we present the concept of a KITWPA operating in a non-degenerate-pump four-wave mixing (NP-4WM) regime, whereby the injection of two pump tones along with a weak signal results in a broad, flat gain profile that removes the zero-gain gap as well as eliminates the need for a DC bias and the complexities associated with it. We demonstrate how a NP-4WM KITWPA is feasible to achieve broadband amplification at a range of frequencies, first in the microwave range where most KITWPAs reported to-date have been successfully experimentally characterised. We then extend the designs to several millimetre (mm) bands to illustrate how we can use this technique to design a broadband front-end pre-amplifier that covers several Atacama Large Millimetre/sub-millimetre Array (ALMA) Bands.

1. Introduction

Broadband amplifiers with quantum-limited noise performance and low power consumption are crucial for applications involving ultra-sensitive cryogenic detection systems such as astronomical receivers [1–3], axion dark matter search experiments [4–6], and quantum computation [7–9]. Kinetic inductance travelling-wave parametric amplifiers (KITWPAs) [10–14] are quantum devices, which can achieve high gain over broad bandwidth by efficiently transferring power from a strong pump wave to the detected weak signal wave via the wave mixing mechanisms in a non-linear medium comprising a high kinetic inductance wire. They are typically realised as a long superconducting transmission line utilising high normal resistivity films. They have been experimentally verified to exhibit near quantum-limited noise performance [15] with negligible heat dissipation, whilst their ease of fabrication compared to other amplifier types, such as Josephson-junction travelling-wave parametric amplifiers (JTWPAs), makes them readily scalable to arrays for large pixel count applications, such as the readout of astronomical detector arrays and realistic large scale quantum computation platforms.

KITWPAs are still relatively young in their development process, and are yet to see widespread use in scientific experimental setups due to a number of operational obstacles that must be overcome, such as ripples in the gain profile, the complicated pump injection and separation, signal-idler contamination, their reciprocity, and the zero-gain gap at the centre gain profile. In this paper, we address the issue of the zero-gain gap, with particular focus on high-frequency KITWPAs where they have the potential to be used for applications such as

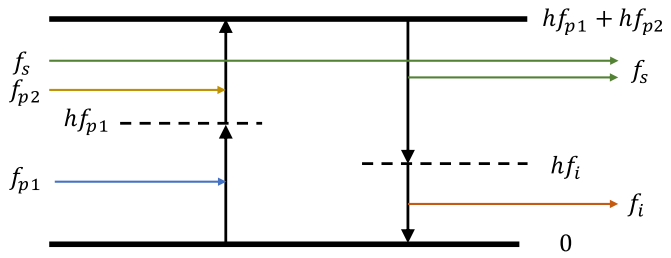

Figure 1. Energy diagram for non-degenerate-pump four-wave mixing (NP-4WM), where h is the Planck constant. In this process, two pump photons at frequencies f_{p_1} and f_{p_2}, respectively, are converted into a signal photon at frequency, f_s and an idler photon at f_i.

front-end receivers for mm/sub-mm astronomy [1]. The remaining issues are to be discussed further in an upcoming publication.

Early KITWPA designs amplified a signal at frequency, f_s, using a single pump tone at frequency, f_p, which promotes a degenerate-pump four-wave mixing (DP-4WM) mode and produces an idler tone at frequency, $f_i = 2f_p - f_s$ [10, 11, 13]. Whilst simple to design and operate, the main downside to such a scheme is that the necessary dispersion engineering that is required to satisfy the phase-matching condition results in a large zero-gain gap in the centre of the gain profile, which also limits the operational frequency range of the KITWPA. Additionally, the design simplicity is countered by the fact that the strong pump tone at the centre of the gain profile must be removed before the subsequent signal processing chain in order to prevent saturation of the microwave components following the KITWPA, such as the cryogenic low-noise amplifiers (LNAs). For example, in actual operation of a KITWPA, one needs to utilise a separate, phase-shifted pump tone to eliminate the original pump, which demands additional RF components [16] and takes up valuable space in a cryogenic environment. This solution may also incur additional unwanted losses in the detection chain, not to mention complicating the experimental setup. The pump tone can also be removed via the use of filters placed after the KITWPA, although it is difficult to engineer the frequency response of a filter to suppress the pump tone alone without sacrificing any of the signal band.

In more recent designs, the KITWPA was biased with a DC current, which was applied along with the pump tone to operate the device in a DC-biased three-wave mixing (DC-3WM) mode [12, 14, 15], with the idler now generated at $f_i = f_p - f_s$. The advantage of such a scheme is that the pump is now shifted to twice the centre frequency of the gain profile, hence displaces the zero-gain gap from the centre of the gain profile to the edges. This means that the pump can now be removed with an additional filter or a diplexer without reducing the operational bandwidth of the KITWPA. In practice, the need for a DC current means additional bias tees and DC lines are required, which complicates the experimental setup. Additionally, the requirement for the pump tone to be at double the centre frequency of the amplifier gain band is inconvenient, as the maximum frequency specification of the external RF cabling network and the finite bandwidth over which the transmission line is matched to 50Ω makes it more difficult to efficiently couple the pump power to the signal tone for DC-3WM; a property that is exacerbated at higher operational frequencies. It is, therefore, desirable for the pump frequency (ies) to be as close to the gain band as possible without lying within it.

To overcome the operational restrictions of these regimes, we introduce here a KITWPA working in a non-degenerate-pump four-wave mixing (NP-4WM) mode, whereby we inject two separate pump tones at frequencies f_{p_1} and f_{p_2}, respectively, along with the signal tone, which subsequently generates an idler with frequency, $f_i = f_{p_1} + f_{p_2} - f_s$, as highlighted by the energy diagram shown in figure 1. The advantages of such a wave mixing regime is that we are able to eliminate the zero-gain gap in the gain profile, whilst maximising the total bandwidth of the device, as the two pump tones can be placed just to the upper and lower edges of the gain profile such that they can be removed easily with a band-pass filter. This wave mixing regime has previously been experimentally verified using JTWPAs [17, 18] and in the optical regime [19, 20]. In this paper, we extend the concept to KITWPAs and demonstrate how a NP-4WM KITWPA could be a feasible solution for high frequency amplification by presenting a series of KITWPA designs, which could potentially be used to enhance the performance of many currently available millimetre (mm) instruments such as the various mm receivers of the Atacama Large Millimetre/sub-millimetre Array (ALMA).

2. Theory

As stated, NP-4WM KITWPA operation involves coupling the detected weak signal along with two pump tones at two distinct frequencies into a long superconducting transmission line (STL). The behaviour of these tones

propagating along the STL, including the generated idler, can be described by a set of coupled ordinary differential equations, known as the coupled-mode equations (CMEs) [21]. Here, we derive the CMEs for NP-4WM, showing that they are in fact the general form which can be further reduced to describe other wave mixing regimes i.e., the DP-4WM and DC-3WM schemes, as special cases to this model.

We begin the derivation of the generalised CMEs with the telegrapher equations [22],

$$\frac{\partial V}{\partial z} = -RI - L\frac{\partial I}{\partial t}, \tag{1}$$

$$\frac{\partial I}{\partial z} = -GV - C\frac{\partial V}{\partial t}, \tag{2}$$

which describe the current, I, and voltage, V, in a transmission line with a series inductance per unit length, L, shunt capacitance per unit length, C, series resistance per unit length, R, and a shunt conductance per unit length, G.

In an STL, the total inductance of the line contains the contributions from both the kinetic inductance of the superconducting film, L_{k}, which arises from the inertia of the moving Cooper pair carriers in the STL, and the geometric inductance, L_{g}, which is dependent on the geometry of the STL. The relationship between L_{k} and I, in the low current limit, can be approximated by a quadratic relation, hence the total inductance per unit length can be given by,

$$L = L_{\mathrm{k0}}\left(1 + \frac{I^2}{I_*^2}\right) + L_{\mathrm{g}}, \tag{3}$$

where L_{k0} is the zero-current kinetic inductance per unit length and I_* is a scaling term that sets the strength of the non-linearity.

Substituting (3) into (1)-(2), then differentiating and rearranging the equations, produces a non-linear wave equation,

$$\begin{aligned}\frac{\partial^2 I}{\partial z^2} = {} & RGI + (L_0 G + RC)\frac{\partial I}{\partial t} + L_{k0} G\frac{I^2}{I_*^2}\frac{\partial I}{\partial t} \\ & + L_0 C\frac{\partial^2 I}{\partial t^2} + L_{k0} C\frac{\partial}{\partial t}\left[\frac{I^2}{I_*^2}\frac{\partial I}{\partial t}\right],\end{aligned} \tag{4}$$

which describes the behaviour of a current propagating along the low-loss STL with a current-dependent kinetic inductance, where $L_0 = L_{\mathrm{k0}} + L_{\mathrm{g}}$. To obtain the CMEs from the wave equation, we can substitute in an ansatz of the form,

$$I = \frac{1}{2}\sum_{\mathrm{j}} A_{\mathrm{j}}(z) e^{i\omega_{\mathrm{j}} t - \gamma_{\mathrm{j}} z} + c.c.\,, \tag{5}$$

which is the sum of all the current contributions of the four tones propagating along the line, where A_{j} is the slowly varying complex amplitude of the component, ω_{j} is the (angular) frequency of the component, $\gamma_{\mathrm{j}} = \alpha_{\mathrm{j}} + i\beta_{\mathrm{j}}$ is the complex propagation constant, $\mathrm{j} = \mathrm{p}_1, \mathrm{p}_2, \mathrm{s}, \mathrm{i}$ signify the two pumps, signal, and idler components, respectively, and *c. c.* denotes the complex conjugate.

The substitution of (5) into (4) can be simplified by using the slowly varying envelope approximation, $\left|\frac{d^2 A_{\mathrm{j}}}{dz^2}\right| \ll \left|\gamma_{\mathrm{j}}\frac{dA_{\mathrm{j}}}{dz}\right|$ and the relation, $\gamma = \sqrt{(R + i\omega L)(G + i\omega C)}$. Performing the substitution results in a large number of cross-terms that requires a non-trivial amount of algebraic manipulation, which can be computed using an algebra manipulation software such as Mathematica. Collecting the relevant terms that oscillate at the same frequencies, and following the procedure described in [23, 24], results in a set of four coupled differential equations,

$$\begin{aligned}\frac{dA_{\mathrm{p_1}}}{dz} = {} & \frac{\omega_{\mathrm{p_1}}^2 L_{\mathrm{k0}} C\eta_{\mathrm{p_1}}}{8\gamma_{\mathrm{p_1}} I_*^2}[(\epsilon_{\mathrm{p_1,\,p_2}} e^{-(\gamma_{\mathrm{p_1}} + \gamma_{\mathrm{p_1}}^*)z}|A_{\mathrm{p_1}}|^2 \\ & + 2e^{-(\gamma_{\mathrm{p_2}} + \gamma_{\mathrm{p_2}}^*)z}|A_{\mathrm{p_2}}|^2 + 2e^{-(\gamma_{\mathrm{s}} + \gamma_{\mathrm{s}}^*)z}|A_{\mathrm{s}}|^2 \\ & + 2e^{-(\gamma_{\mathrm{i}} + \gamma_{\mathrm{i}}^*)z}|A_{\mathrm{i}}|^2)A_{\mathrm{p_1}} \\ & + 2e^{(\gamma_{\mathrm{p_1}} - \gamma_{\mathrm{p_2}}^* - \gamma_{\mathrm{s}} - \gamma_{\mathrm{i}})z} A_{\mathrm{i}} A_{\mathrm{s}} A_{\mathrm{p_2}}^*],\end{aligned} \tag{6a}$$

$$\frac{dA_{p_2}}{dz} = \frac{\omega_{p_2}^2 L_{k0} C \eta_{p_2}}{8\gamma_{p_2} I_*^2}[(\epsilon_{p_1,\,p_2} e^{-(\gamma_{p_2}+\gamma_{p_2}^*)z}\,|A_{p_2}|^2 + 2e^{-(\gamma_s+\gamma_s^*)z}\,|A_s|^2 + 2e^{-(\gamma_i+\gamma_i^*)z}\,|A_i|^2 + 2e^{-(\gamma_{p_1}+\gamma_{p_1}^*)z}\,|A_{p_1}|^2)A_{p_2} + 2e^{(\gamma_{p_2}-\gamma_{p_1}^*-\gamma_s-\gamma_i)z}A_i A_s A_{p_1}^*], \tag{6b}$$

$$\frac{dA_s}{dz} = \frac{\omega_s^2 L_{k0} C \eta_s}{8\gamma_s I_*^2}[(e^{-(\gamma_s+\gamma_s^*)z}\,|A_s|^2 + 2\epsilon_{p_1,\,p_2} e^{-(\gamma_{p_2}+\gamma_{p_2}^*)z}\,|A_{p_2}|^2 + 2e^{-(\gamma_i+\gamma_i^*)z}\,|A_i|^2 + 2\epsilon_{p_1,\,p_2} e^{-(\gamma_{p_1}+\gamma_{p_1}^*)z}\,|A_{p_1}|^2)A_s + 2\epsilon_{p_1,\,p_2} e^{(\gamma_s-\gamma_i^*-\gamma_{p_1}-\gamma_{p_2})z}A_i^* A_{p_1} A_{p_2}], \tag{6c}$$

$$\frac{dA_i}{dz} = \frac{\omega_i^2 L_{k0} C \eta_i}{8\gamma_i I_*^2}[(e^{-(\gamma_i+\gamma_i^*)z}\,|A_i|^2 + 2\epsilon_{p_1,\,p_2} e^{-(\gamma_{p_1}+\gamma_{p_1}^*)z}\,|A_{p_1}|^2 + 2\epsilon_{p_1,\,p_2} e^{-(\gamma_{p_2}+\gamma_{p_2}^*)z}\,|A_{p_2}|^2 + 2e^{-(\gamma_s+\gamma_s^*)z}\,|A_s|^2)A_i + 2\epsilon_{p_1,\,p_2} e^{(\gamma_i-\gamma_s^*-\gamma_{p_1}-\gamma_{p_2})z}A_s^* A_{p_1} A_{p_2}], \tag{6d}$$

which are the generalised CMEs, where $\eta_j = \left(1 - i\frac{G}{\omega_j C}\right)$ and,

$$\epsilon_{p_1,\,p_2} = \begin{cases} 2 & for \omega_{p_1} = \omega_{p_2} \\ 1 & otherwise \end{cases} \tag{7}$$

Assuming that the amplitude of any pump harmonics or other mixing terms are either very small or suppressed via dispersion engineering (discussed further in Appendix C), (6a)-(6d) in fact describe a general framework that can be configured to cover the different wave mixing schemes, as well as including the losses that the pumps, signal, and idler experience whilst travelling along the line. There are some approximations, however, that we can make to (6a)-(6d) to simplify their solution. As KITWPAs require superconducting films, such as titanium nitride (TiN) or niobium titanium nitride (NbTiN) that exhibit very high kinetic inductance, we can assume that $L_k \gg L_g$, hence $L_0 = L_{k0} + L_g \approx L_{k0}$. We can also assume operation in the low-loss limit with the use of superconducting films, hence the complex propagation constant can be Taylor expanded and approximated as $\gamma \approx i\omega\sqrt{LC}\left[1 - \frac{i}{2}\left(\frac{R}{\omega L} + \frac{G}{\omega C}\right)\right]$. This is further justified as most KITWPA transmission lines comprises a STL fabricated onto a high resistivity or ceramic substrate such as silicon or sapphire, hence we can assume that R and G are very small compared to L and C, respectively. Additionally, as we are operating at high frequencies, the relation $G \ll \omega C$ applies, so $\eta_j \approx 1$ for all j.

With these assumptions, (6a)-(6d) reduce to,

$$\frac{dA_{p_1}}{dz} = \frac{\beta_{p_1}^2}{8\gamma_{p_1} I_*^2}[(\epsilon_{p_1,\,p_2} e^{-(\gamma_{p_1}+\gamma_{p_1}^*)z}\,|A_{p_1}|^2 + 2e^{-(\gamma_{p_2}+\gamma_{p_2}^*)z}\,|A_{p_2}|^2 + 2e^{-(\gamma_s+\gamma_s^*)z}\,|A_s|^2 + 2e^{-(\gamma_i+\gamma_i^*)z}\,|A_i|^2)A_{p_1} + 2e^{(\gamma_{p_1}-\gamma_{p_2}^*-\gamma_s-\gamma_i)z}A_i A_s A_{p_2}^*], \tag{8a}$$

$$\frac{dA_{p_2}}{dz} = \frac{\beta_{p_2}^2}{8\gamma_{p_2} I_*^2}[(\epsilon_{p_1,\,p_2} e^{-(\gamma_{p_2}+\gamma_{p_2}^*)z}\,|A_{p_2}|^2 + 2e^{-(\gamma_s+\gamma_s^*)z}\,|A_s|^2 + 2e^{-(\gamma_i+\gamma_i^*)z}\,|A_i|^2 + 2e^{-(\gamma_{p_1}+\gamma_{p_1}^*)z}\,|A_{p_1}|^2)A_{p_2} + 2e^{(\gamma_{p_2}-\gamma_{p_1}^*-\gamma_s-\gamma_i)z}A_i A_s A_{p_1}^*], \tag{8b}$$

$$\frac{dA_s}{dz} = \frac{\beta_s^2}{8\gamma_s I_*^2}[(e^{-(\gamma_s+\gamma_s^*)z}\,|A_s|^2 + 2\epsilon_{p_1,\,p_2}e^{-(\gamma_{p_2}+\gamma_{p_2}^*)z}\,|A_{p_2}|^2 + 2e^{-(\gamma_i+\gamma_i^*)z}\,|A_i|^2 + 2\epsilon_{p_1,\,p_2}e^{-(\gamma_{p_1}+\gamma_{p_1}^*)z}\,|A_{p_1}|^2)A_s + 2\epsilon_{p_1,\,p_2}e^{(\gamma_s-\gamma_i^*-\gamma_{p_1}-\gamma_{p_2})z}A_i^* A_{p_1}A_{p_2}], \tag{8c}$$

$$\frac{dA_i}{dz} = \frac{\beta_i^2}{8\gamma_i I_*^2}[(e^{-(\gamma_i+\gamma_i^*)z}\,|A_i|^2 + 2\epsilon_{p_1,\,p_2}e^{-(\gamma_{p_1}+\gamma_{p_1}^*)z}\,|A_{p_1}|^2 + 2\epsilon_{p_1,\,p_2}e^{-(\gamma_{p_2}+\gamma_{p_2}^*)z}\,|A_{p_2}|^2 + 2e^{-(\gamma_s+\gamma_s^*)z}\,|A_s|^2)A_i + 2\epsilon_{p_1,\,p_2}e^{(\gamma_i-\gamma_s^*-\gamma_{p_1}-\gamma_{p_2})z}A_s^* A_{p_1}A_{p_2}], \tag{8d}$$

which are the CMEs used to calculate the KITWPA gain profiles throughout this paper, where $\beta_j \equiv \Im[\gamma_j]$.

Additionally, this set of CMEs can be reformed straightforwardly into the CMEs for the other two distinct wave mixing regimes discussed in this paper as special cases. For example, by making the substitutions $\omega_{p_1} = \omega_{p_2} = \omega_p$ and $A_{p_1} = A_{p_2} = \frac{A_p}{2}$, (6a)–(6d) reduce to the CMEs for DP-4WM. Alternatively, if we make the substitutions, $\omega_{p_1} = \omega_p$, $\omega_{p_2} = 0$, and $A_{p_1} = A_p$, $A_{p_2} = I_{DC}$, (6a)–(6d) reduce to the CMEs for DC-3WM. The detailed derivation for this is presented in the appendices.

3. Design considerations

In this section, we present the design of a NP-4WM KITWPA, making use of a design centred at 9 GHz as an example. To illustrate the advantages of a NP-4WM KITWPA, we compare the behaviour of the NP-4WM design to a standard DP-4WM KITWPA, including some additional design considerations. As stated in [10], the non-linearity of the transmission line forming the KITWPA naturally leads to a phase-mismatch between the various propagating tones that needs correcting in order to maximise the gain. Furthermore, harmonics of the pump tone are also generated in the non-linear medium, which require suppression in order to prevent shock-wave formation [25] and to ensure maximum power transfer from the pump to the signal tone. Both of these effects would exist in a KITWPA regardless of the operational mode i.e., DP-4WM or DC-3WM, and can be suppressed via a technique called the dispersion engineering, where stopbands are created in the dispersion relation of the KITWPA by periodically modulating the impedance of the transmission line along its length with discretely loaded short sections [10, 24, 26, 27].

The same would be required for a NP-4WM KITWPA, however, there are more considerations needed to be taken into account to ensure proper operation with two pump tones. Figure 2 compares the pump harmonics generated for DP-4WM, DC-3WM, and NP-4WM devices. For DP-4WM in figure 2(a), a strong third harmonic of the pump tone would be generated due to the Kerr-3 non-linearity of the superconducting transmission line, which is followed by further, subsequent odd harmonics of the pump tone. This is similar for the case of DC-3WM in figure 2(b), except now odd and even harmonics are both generated in this operational mode. For the NP-4WM case illustrated in figure 2(c), we see that the two pump tones both create odd harmonics of themselves, with the added complexity arising from the numerous cross terms generated by the two pumps interacting with each other. In DP-4WM, suppressing the third harmonic is sufficient to suppress all further harmonics and to prevent shock-wave formation, which can easily be achieved by introducing periodic stopbands starting at $3f_p$. For the NP-4WM case, however, this becomes extremely difficult as there are now many harmonics and cross terms that are not placed periodically. As we will discuss later, however, there are some particular configurations of the NP-4WM regime that would allow for convenient suppression of all the unwanted harmonics.

3.1. Harmonics suppression

Although figure 2(c) shows that the pump harmonics are positioned irregularly in the NP-4WM mode, there are indeed cases where they can be lined up periodically, which allows the harmonic suppression mechanism to more easily utilise the standard periodic loading technique. Consider the case where we inject the two pump tones into the KITWPA with the second pump having approximately double the frequency of the first pump tone i.e., $f_{p_2} \approx 2 \times f_{p_1}$ as example. Table 1 summarises the first few generated harmonics when the two pump tones are injected into a KITWPA with $f_{p_1} = 6$ GHz and $f_{p_2} = 12$ GHz. We notice that in this case, the harmonics are in fact all generated at integer multiples of 6 GHz, which provides us with a convenient solution i.e., we can engineer our periodic loading structures to create stopbands in the transmission profile at integer

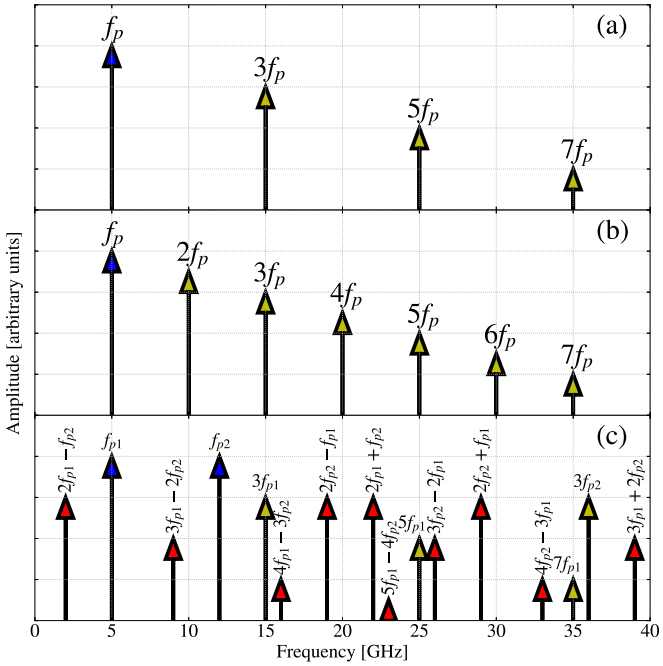

Figure 2. An illustrative comparison of the pump harmonics generated for DP-4WM (a), DC-3WM (b), and NP-4WM (c). The blue arrows indicate the the incoming pump tones, the yellow arrows indicate the harmonics of the pump tones and the red arrows indicate the cross-harmonics between the pump tones in NP-4WM.

Table 1. Frequencies of the pump tones and their harmonics for NP-4WM in the case where $f_{P_1} = 6$ GHz and $f_{P_2} = 12$ GHz.

Term	Frequency [GHz]
f_{P_1}	6
f_{P_2}	12
$2f_{P_1} - f_{P_2}$	0
$2f_{P_2} - f_{P_1}$	18
$3f_{P_1}$	18
$2f_{P_1} + f_{P_2}$	24
$2f_{P_2} + f_{P_1}$	30
$3f_{P_2}$	36
$3f_{P_1} - 2f_{P_2}$	6
$3f_{P_2} - 2f_{P_1}$	24
$3f_{P_1} + 2f_{P_2}$	42
$3f_{P_2} + 2f_{P_1}$	48
$4f_{P_1} - 3f_{P_2}$	12
$4f_{P_2} - 3f_{P_1}$	30
$4f_{P_1} + 3f_{P_2}$	60
$4f_{P_2} + 3f_{P_1}$	66
$5f_{P_1} - 4f_{P_2}$	18

multiples of 6 GHz. Placing the two pump tones on the edge of the first and second stopbands, respectively, will result in them acquiring the additional phase shift required for phase matching, while the harmonics of the pump tones will be attenuated by the larger subsequent stopbands at 18, 24, 30, 36 GHz etc.

To demonstrate the feasibility of this configuration, here we present a 6–12 GHz NP-4WM KITWPA design simulated using the procedure described in [24]. Figure 3 shows a drawing of the KITWPA design, which comprises an inverted microstrip transmission line comprising 650 unit cells to give a total transmission line length of 49.6mm. The 250 nm wide inverted microstrip is formed with a wiring layer of 35 nm NbTiN (normal-

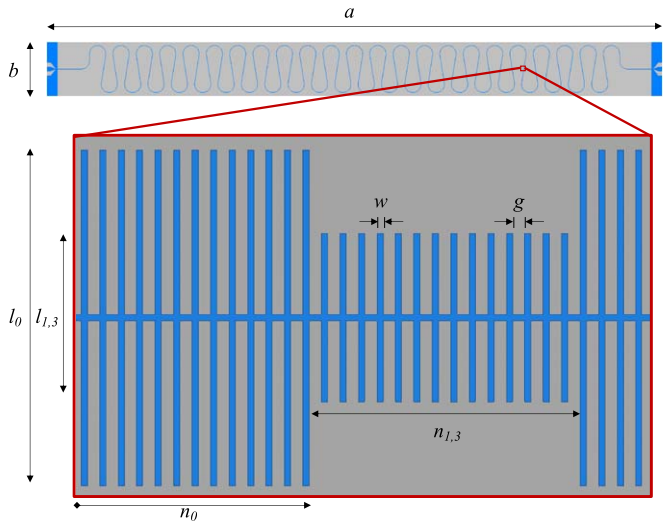

Figure 3. Layout of the 6–12 GHz KITWPA design showing the wiring layer (blue) of the inverted microstrip, which is wound into a 'hairpin' pattern to fit the design onto a compact configuration. The substrate is shown in grey and the dielectric and sky planes are not shown for clarity. The inset highlights one of the periodic loading sections of the transmission line.

Table 2. Summary of physical design parameters for the 6–12 GHz NP-4WM KITWPA.

Description	Parameter	Value
Chip length	a	40.0 mm
Chip width	b	3.0 mm
Microstrip width	w	250 nm
Stub gap	g	500 nm
Stub length (50 Ω)	l_0	13.0 μm
Stub length (1st loading)	l_1	8.8 μm
Stub length (3rd loading)	l_3	6.4 μm
No. of stubs (50 Ω section)	n_0	82
No. of stubs (1st loading)	n_1	10
No. of stubs (3rd loading)	n_3	10
Total no. of cells	n_{tot}	650

state resistivity, $\rho_{\mathrm{N}} = 200\ \mu\Omega$ cm and critical temperature, $T_{\mathrm{c}} = 15$ K), which is deposited onto a 675 μm thick high-resistivity silicon substrate. The wiring layer is then covered by a 100 nm-thick amorphous silicon (a-Si) dielectric, topped by another 200 nm Nb sky-plane.

To achieve a 50 Ω transmission line, the conducting strip of the inverted microstrip is shunted with additional stubs, which increase the capacitance per unit length to balance the high kinetic inductance of the NbTiN film. To create the desired stopbands, periodic loadings sections were created by altering the characteristic impedance of the transmission line by changing the length of the shunted stubs as shown in the inset of figure 3. The physical dimensions of the transmission line making up the KITWPA are summarised in table 2.

Figure 4 shows the simulated $|S_{21}|$ transmission spectrum for the 6–12 GHz NP-4WM device showing the stopbands at the integer multiples of ~6 GHz, as generated by the periodic loadings. With the placement of $f_{\mathrm{p_1}} = 6.148$ GHz and $f_{\mathrm{p_2}} = 12.30$ GHz pumps on the leading edges of the first and second stopbands, respectively, we show that the pump harmonics and their cross-terms would fall into the subsequent stopbands at higher frequencies. The $|S_{21}|$ spectrum presented here has been simulated using the realistic modelling technique described in [24], which has been shown to accurately predict the measured performance of KITWPAs when the surface resistance of the superconducting film is calibrated to be close to negligible compared to the BCS prediction [28] at cryogenic temperature. Figure 5(a) shows the gain-bandwidth profile for the KITWPA, which was calculated by numerically solving the CMEs in (8a)–(8d), and demonstrates a gain greater than 20 dB over the frequency band from 6–12 GHz with the pump currents set at $I_{\mathrm{p_1}} = I_{\mathrm{p_2}} = 0.0725 I_*$.

Comparing this gain curve to an equivalent DP-4WM KITWPA operating in the same frequency range, we can see a number of improvements in the NP-4WM curve. First, the gain of the NP-4WM KITWPA remains

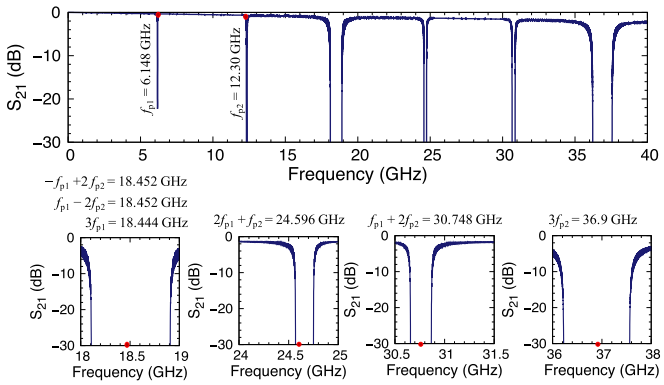

Figure 4. Transmission spectrum of the 6–12 GHz NP-4WM KITWPA, highlighting the positions of the pump tones and the generated harmonics, which can be suppressed by the engineered higher frequency stopbands.

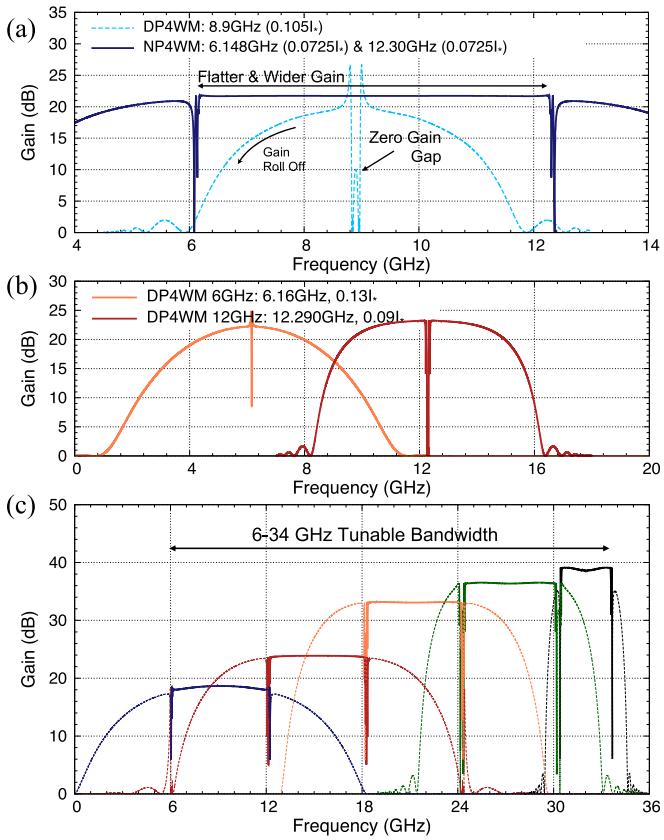

Figure 5. (a) Gain-bandwidth profile for a KITWPA operating in the NP-4WM regime (dark blue) highlighting the broad, flat gain profile compared to a DP-4WM KITWPA (light blue) operating in the same frequency range. (b) DP-4WM gain-bandwidth profiles for the 6–12 GHz KITWPA design, highlighting how this design is not restricted to operation in the NP-4WM mode. (c) Gain profiles of the continuously tunable 6–34 GHz NP-4WM TWPA.

roughly constant over the targeted band, which is in stark contrast to the DP-4WM gain curve where the gain rolls off severely towards the edges of the band i.e., the target gain of 20 dB is only achieved for a very small region towards the centre of the gain profile. Second, the NP-4WM curve also eliminates the central zero-gain region. Additionally, the NP-4WM device can also be operated in the DP-4WM mode, as shown in figure 5(b), to cover bandwidth below 6 GHz and above 12 GHz, albeit with the pump frequencies and currents tuned to satisfy the different phase matching conditions for the DP-4WM mode.

It should be noted that whilst the previous analysis explained that we have chosen a regime where $f_{p_2} = 2f_{p_1}$, there is in fact some tolerance in this, i.e., it is not crucial that f_{p_2} is exactly double f_{p_1}, just that it is close to it. In this particular example, therefore, we have tuned the pump values to $f_{p_1} = 6.148$ GHz and $f_{p_2} = 12.30$ GHz as

this produces the optimum phase matching and the desired gain performance, yet the pump harmonics and cross terms are still attenuated by the engineered stopbands.

A further advantage of this dual-pump configuration is the possibility to substantially widen the bandwidth by re-configuring the frequencies of the pump tones, similar to pumping at different stopbands in the DP-4WM scheme. As the periodic loading creates stopbands at the integer multiples of ∼6 GHz, we can place the pump tones on the edges of different stopbands to operate our KITWPA over different frequency bands. This is demonstrated in figure 5(c) where we alter the width of every sixth loading section instead of every third, and show how the pump frequencies can be adjusted to potentially produce an enormous continuous 6–34 GHz tunable bandwidth of the KITWPA using exactly the same design as presented figure 3.

4. Millimetre wave TWPA

In section 3 we presented the design for a microwave NP-4WM KITWPA operating over the frequency range 6–12 GHz. Despite the many advantages this design presents over a KITWPA operating in the DP-4WM regime, it remains that the DC-3WM KITWPA could offer similar broadband performance apart from the roll-off of the gain profile near the edges of the band, and the need for a DC-biasing current. However, at higher operational frequencies such as in the regime of mm/sub-mm wavelength, the use of a DC-3WM KITWPA may become challenging with the need for DC-biasing current that may also incur additional heating effect through the DC wires to the cryogenic stages. In this sense, we argue that the main avenue where a NP-4WM KITWPA is most advantageous compared to other options is when the KITWPA is needed for high-frequency operation beyond the microwave range, where RF signal transmission is reliant on waveguides instead of coaxial cabling. At these high frequencies, the non-linear dispersion of the STL inevitably becomes stronger as the signal frequency becomes a significant fraction of the superconducting gap frequency. In this section, we present a series of NP-4WM designs operating at mm-wave frequencies covering ALMA Bands 1–5 to demonstrate this advantage, along with several other design considerations required for KITWPA operating in a waveguide environment.

4.1. ALMA band-1 KITWPA

ALMA Band-1 covers a frequency range of 35–50 GHz [29], and is currently the lowest frequency band in operation at the ALMA observatory. The current technology used in the Band-1 signal detection scheme utilises high electron mobility transistor (HEMT) amplifiers as first-stage detectors with a receiver noise temperature approaching 32K [29], which is still slightly higher than the ultimate quantum noise limit.

Within the Band-1 range, it is in principle possible to drive the first-stage amplifier via 'v'-connectors rated for operation up to 70 GHz. This implies that it is possible to replace the HEMT amplifiers with DC-3WM KITWPAs, providing that similarly broadband bias-tees are available. However, this also requires the pump frequency to be set at least twice the centre frequency of the gain profile i.e., close to 90 GHz. But a pump at such high frequency is beyond the operational range of 'v'-connectors, hence the operation of Band-1 TWPA may require the entire ALMA Band-1 RF-signal cabling network be replaced with 1.35 mm or 1.0 mm ('w') connectors, which complicates the design and increases the cost. Even if one replaces the coaxial connections with waveguides, it is still very challenging to construct an ultra broadband waveguide probe antenna that can cover such wide (close to 3:1) bandwidth. Given that the pump frequencies for a NP-4WM KITWPA are much closer to the operational bandwidth, it implies that both the signal and the pumps can be transmitted using either a common coaxial cable or a waveguide probe with reasonable bandwidth performance.

We present here a NP-4WM KITWPA designed to cover the ALMA Band-1 range using the 'v'-type coaxial connection similar to the design shown earlier in figure 3. The physical parameters of the Band-1 KITWPA are summarised in table 3 and echo those of table 2. As with the 6–12 GHz design, we use an inverted microstrip structure fabricated from the same 35 nm NbTiN film patterned onto the 675 μm silicon substrate, with a 100 nm a-Si dielectric, and 200 nm Nb sky plane. Figure 6(a) shows the gain-bandwidth profile of the KITWPA with a flat gain over 20 dB that comfortably covers the entire Band-1 bandwidth. The pump currents used to simulate the gain profile are $I_{p_1} = I_{p_2} = 0.075 I_*$ with the pump frequencies $f_{p_1} = 30.0$ GHz and $f_{p_2} = 57.7$ GHz, which in contrast to the DC-3WM case, lie comfortably within the frequency specification of 'v'-connectors. Figure 6(b) shows the $|S_{21}|$ transmission profile and the non-linear dispersion (β_{nl}, the wavevector of the non-linear line that diverges away from the otherwise linear relation) of the line, highlighting the positions for the pump tones and the generated harmonics. One will notice that unlike the 6–12 GHz KITWPA, the pump harmonics do not line up exactly with the stopbands. This example was shown here on purpose to demonstrate that there is indeed another design scheme that one could utilise to produce an operable NP-4WM KITWPA.

One may have noticed from table 3 that in this example, we do not alter the stub length to be abruptly difference from that of the 6–12 GHz design. In section 3, we explained that the use of stubs shunted to the main

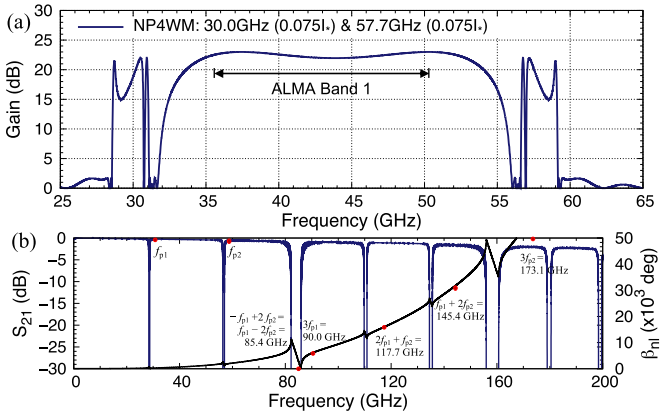

Figure 6. (a) Gain and (b) $|S_{21}|$ transmission and the non-linear dispersion characteristic of ALMA Band-1 NP-4WM KITWPA.

Table 3. Summary of physical design parameters for ALMA Band-1 KITWPA.

Description	Parameter	Value
Chip length	a	6.5 mm
Chip width	b	2.0 mm
Microstrip width	w	250 nm
Stub gap	g	500 nm
Stub length (50 Ω)	l_0	12.8 μm
Stub length (1st loading)	l_1	9.0 μm
Stub length (3rd loading)	l_3	4.8 μm
No. of stubs (50 Ω section)	n_0	18
No. of stubs (1st loading)	n_1	2
No. of stubs (3rd loading)	n_3	2
Total no. of cells	n_{tot}	500

conductor line allowed for 50 Ω impedance matching, however, they have an additional effect i.e., creating a resonance frequency at the very high frequency end of the transmission spectrum, which in this example is near to 450 GHz for a stub length of 9 μm. Due to the closeness of the operational frequencies here to the resonance frequency, the non-linear dispersion inevitably diverges away from the otherwise linear relation much more strongly than the case without any stubs. This subsequently results in the high frequency stopbands being packed closer to each other, instead of at integer multiples of the primary stopband. This implies that the scheme described above may not work to suppress the unwanted harmonics. Nevertheless, this highly non-linear dispersion (β_{nl}) would also cause a severe phase mismatch if uncorrected for, hence, we can make use of this property to prevent the unwanted harmonics from being generated. We, therefore, do not need to engineer the harmonics to be placed directly into the stopbands in order to suppress them. It should also be noted that due to this large non-linear dispersion being nearer to the gain band, we actually have to place the pump frequencies above the first two stopbands in order to achieve phase matching and hence the high gain as shown in figure 6.

4.2. ALMA bands 2–5

ALMA Bands 2–5 cover the electromagnetic spectrum over the range of 67–211 GHz [29], and at these frequencies, we can no longer use coaxial cables for signal transmission and are instead reliant on waveguide transmission. DC-biasing a KITWPA mounted within a waveguide may be complicated as a pair of additional DC lines would need to be connected electrically to the chip, which is now much smaller in size at such high frequency. For operation in this range, therefore, NP-4WM is preferable. In this section, we present two designs, which cover the ALMA Bands 2–3 and 4–5, respectively.

As stated earlier, signal coupling using waveguide structure necessitates the design of a waveguide-to-planar circuit transition (or an op-chip antenna). It is, therefore, crucial that the design of the antenna is carried out first, as this sets the limitations and restrictions on the transmission line dimensions and materials, as well as the characteristic impedance of the line, which no longer needs to be matched to a 50 Ω.

Figure 7(a) shows the layout of our antenna designed to couple the pumps and signal to our KITWPA chips, with the physical parameters specified in table 4 for both the Band 2–3 and Band 4–5 KITWPAs. The probe

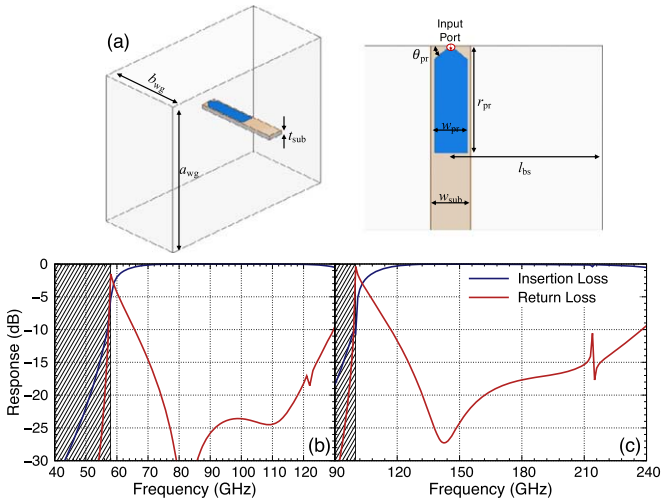

Figure 7. (a) CAD (computer-aided design) model of antenna used in mm NP-4WM KITWPA, with parameters specified in table 4. Antenna bandwidth for Band 2–3 (b) and Band 4-5 (c) designs.

Table 4. Summary of physical design parameters for ALMA Band 2–5 KITWPA antennae.

Band	60–120 GHz	120–240 GHz
a_{wg} (mm)	2.60	1.50
b_{wg} (mm)	1.30	0.65
l_{bs} (mm)	0.80	0.42
t_{sub} (μm)	80.0	40.0
w_{sub} (μm)	216.2	115.6
r_{pr} (μm)	690.0	380.0
w_{pr} (μm)	196.2	95.6
θ_{pr} (°)	41.7	45.4
Z_{ant} (Ω)	70.6	67.7

antenna is expected to be formed using the same 35 nm NbTiN film used in previous designs, except it is now deposited onto a 80 μm thick quartz substrate for the Band 2–3 and 40 μm for the Band 4–5 design, as the lower dielectric constant provides a better coupling to the antenna compared to a higher dielectric constant silicon substrate. Figure 7(b) and figure 7(c) show the antenna bandwidth for the Band 2–3 and Band 4–5 designs, respectively. One immediately notices the finite bandwidth of the antenna, which makes it difficult to couple a pump tone to the KITWPA at twice the central frequency, hence making operation in the DC-3WM mode challenging.

Having designed the KITWPA antennae, we can now proceed to the design of the KITWPA itself. From table 4, we notice that the output impedance for both antennae is approximately 70 Ω, meaning that we would need to match the characteristic impedance of the main sections of the TWPA itself to this value, instead of the usual 50 Ω. Figure 8 shows a drawing of the KITWPA design used for both frequency bands, which are identical in form except the physical dimensions vary between each design, as summarised in table 5. Contrary to the lower frequency KITWPA devices, these devices comprise a regular (non-inverted) microstrip design, which is formed by depositing a 200 nm ground plane onto an 80 μ m quartz substrate for the Band 2–3 and a 40 μm quartz substrate for the Band 4–5 design, followed by a 100 nm a-Si dielectric, which is topped by the 35 nm NbTiN wiring layer. The reason for swapping the inverted microstrip structure with a regular microstrip is because with such a thin substrate with lower dielectric constant, when the device is mounted into a metallic block, the inverted microstrip line would support a stripline propagation mode as the current carrying line now 'sees' the metallic surface as another 'ground' plane. This mode has a completely different characteristic impedance to the microstrip propagation mode, hence virtually no power would be coupled into the transmission line from the antenna.

Additionally, one will notice from figure 8 that the Band 2–5 microstrips do not use the shunted stubs to achieve the desired impedance, and instead rely solely on the width of the main strip. This is due to the fact that the shunted stubs' resonant frequency alters the transmission profile significantly towards higher frequencies, as

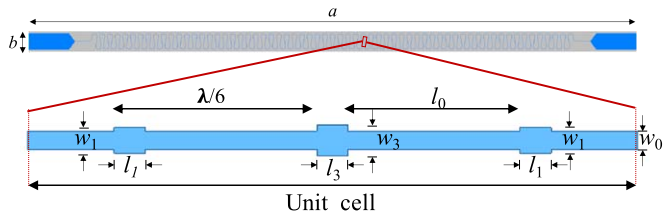

Figure 8. The common layout used for Bands 2–3 & 4–5 KITWPA designs, showing the wiring layer (blue) of the microstrip, which is wound into a 'hairpin' pattern to fit the design onto a single chip. The substrate is shown in grey and the dielectric and ground planes are not shown for clarity. The inset highlights the periodic loading structure of the transmission line.

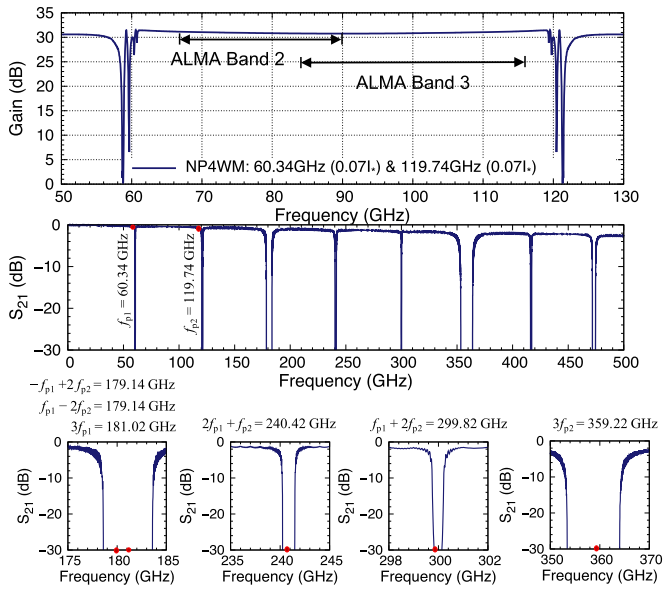

Figure 9. Gain and $|S_{21}|$ transmission of ALMA Band 2–3 KITWPA.

Table 5. Summary of physical design parameters for ALMA Band 2-5 KITWPAs.

Band	60-120 GHz	120-240 GHz
a (mm)	17.5	9.5
b (mm)	2.0	2.0
w_0 (μm)	1.02	1.06
w_1 (μm)	0.18	1.15
w_3 (μm)	1.25	1.19
l_0 (μm)	32.3	16.4
l_1 (μm)	0.6	1.8
l_3 (μm)	3.6	1.8
n_{tot}	500	500

discussed previously, meaning that the use of the stubs would make the KITWPA far too lossy at high frequencies and substantially narrow down the operational bandwidth. Figure 9 shows the gain-bandwidth profile for the Band 2–3 KITWPA device, and clearly shows a relatively flat gain curve above 25 dB over a bandwidth of 60–120 GHz, which comfortably covers the entirety of ALMA Bands 2 and 3. This gain profile is achieved with pump currents of $I_{p_1} = I_{p_2} = 0.07I_*$ and pump frequencies set at $f_{p_1} = 60.34$ GHz and $f_{p_2} = 119.74$ GHz, with the generated harmonic frequencies falling neatly into higher subsequent stopbands.

Similarly, figure 10 shows the gain-bandwidth profile for the Band 4–5 KITWPA device, again showing a flat gain curve above 25 dB over a bandwidth of 120–240 GHz, which comfortably covers the entirety of ALMA Bands 4 and 5, as well as the lower half of Band 6. This gain profile is achieved for pump currents of $I_{p_1} = I_{p_2} = 0.085I_*$ and pump frequencies of $f_{p_1} = 118.0$ GHz and $f_{p_2} = 236.0$ GHz, with the majority of the

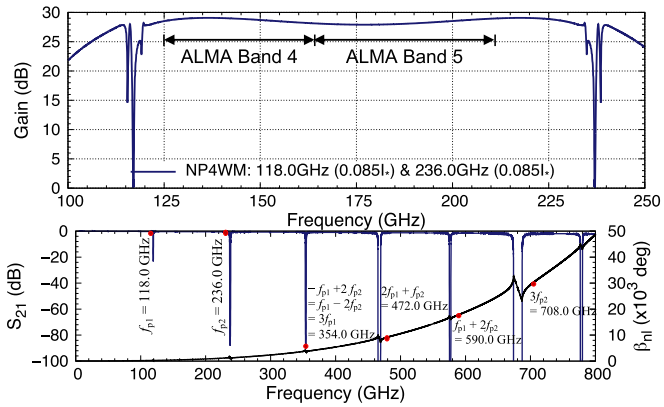

Figure 10. Gain and $|S_{21}|$ transmission and non-linear dispersion profile of the ALMA Band 4-5 KITWPA.

generated harmonic frequencies either falling into the subsequent stopbands or suppressed via the large non-linear dispersion at high frequencies.

5. Conclusion

In this paper, we have presented a series of KITWPA designs operating in the NP-4WM regime, whereby the injection of two pump tones along with a detected signal results in a broad, flat gain profile which removes the zero-gain gap that plagues other KITWPA devices and eliminates the need for a DC bias and the complexities associated with it. We first presented a design concept at microwave frequencies, before extending to mm frequencies, where this solution presents itself as a preferred solution for high mm-wave frequencies compared to the DP-4WM and DC-3WM modes. Work is under progress to fabricate the microwave NP-4WM KITWPAs for experimental verification of the design concept.

Acknowledgments

The authors would like to thank the European Research Council (ERC) programme under the project number 803 862 (SPA4AstroQIT) for supporting this work. For the purpose of Open Access, the author has applied a CC BY public copyright licence to any Author Accepted Manuscript version arising from this submission.
J. Longden's PhD studentship is fully supported by the UK Science and Technology Facilities Council.

Data availability statement

The data that support the findings of this study are available upon reasonable request from the authors.

Appendix A. CME reduction to DP-4WM

Here, we demonstrate how the NP-4WM CMEs in (8a)–(8d) can be reduced to the CMEs for the other wave mixing regimes commonly reported in the literature, beginning with DP-4WM.

As stated, DP-4WM is a particular case of NP-4WM where the two pump tones are equal in frequency and magnitude, and is arguably the most straightforward wave mixing example for a KITWPA. Recall from section 1 that the energy conservation relation for DP-4WM is $2\omega_p = \omega_s + \omega_i$, hence the values of j used for the substituted ansatz are j = p, s, i. The CMEs for DP-4WM can be obtained simply by substituting the DP-4WM specialisation, i.e. $\omega_{p_1} = \omega_{p_2} = \omega_p$ and $A_{p_1} = A_{p_2} = A_p$ into the NP-4WM CMEs. The CMEs in (8a)–(8d), therefore, reduce to the lossy CMEs for DP-4WM,

$$\begin{aligned}\frac{dA_p}{dz} = \frac{\beta_p^2}{8\gamma_p I_*^2}[&(e^{-(\gamma_p+\gamma_p^*)z}\,|A_p|^2 + 2e^{-(\gamma_s+\gamma_s^*)z}\,|A_s|^2 \\ &+ 2e^{-(\gamma_i+\gamma_i^*)z}\,|A_i|^2)A_p \\ &+ 2e^{(\gamma_p-\gamma_p^*-\gamma_s-\gamma_i)z}A_iA_sA_p^*] \end{aligned} \quad (1.1a)$$

$$\frac{dA_s}{dz} = \frac{\beta_s^2}{8\gamma_s I_*^2}[(e^{-(\gamma_s+\gamma_s^*)z}\,|A_s|^2 + 2e^{-(\gamma_i+\gamma_i^*)z}\,|A_i|^2 + 2e^{-(\gamma_p+\gamma_p^*)z}\,|A_p|^2)A_s + e^{(\gamma_s-\gamma_i^*-2\gamma_p)z}A_i^* A_p^2] \tag{1.1b}$$

$$\frac{dA_i}{dz} = \frac{\beta_i^2}{8\gamma_i I_*^2}[(e^{-(\gamma_i+\gamma_i^*)z}\,|A_i|^2 + 2e^{-(\gamma_p+\gamma_p^*)z}\,|A_p|^2 + 2e^{-(\gamma_s+\gamma_s^*)z}\,|A_s|^2)A_i + e^{(\gamma_i-\gamma_s^*-2\gamma_p)z}A_s^* A_p^2], \tag{1.1c}$$

which are equivalent to the CMEs reported in [30].

Taking the fully lossless limit where $\gamma = \alpha + i\beta \to i\beta$ recovers the lossless CMEs for DP-4WM,

$$\frac{dA_p}{dz} = -\frac{i\beta_p}{8I_*^2}[(|A_p|^2 + 2\,|A_s|^2 + 2\,|A_i|^2)A_p + 2A_iA_sA_p^* e^{-i\Delta_\beta^{(D4)}z}] \tag{1.2a}$$

$$\frac{dA_s}{dz} = -\frac{i\beta_s}{8I_*^2}[(|A_s|^2 + 2\,|A_i|^2 + 2\,|A_p|^2)A_s + A_i^* A_p^2 e^{i\Delta_\beta^{(D4)}z}] \tag{1.2b}$$

$$\frac{dA_i}{dz} = -\frac{i\beta_i^2}{8I_*^2}[(|A_i|^2 + 2\,|A_p|^2 + 2\,|A_s|^2)A_i + A_s^* A_p^2 e^{i\Delta_\beta^{(D4)}z}], \tag{1.2c}$$

where $\Delta_\beta^{(D4)} = \beta_s + \beta_i - 2\beta_p$, which are identical to the CMEs reported in [21].

Appendix B. CME reduction to DC-3WM

If a DC signal is passed along the STL, the symmetry of the line is broken and DC-3WM mode can take place. Recall from section 1 that the energy conservation relation for DC-3WM is $\omega_p = \omega_s + \omega_i$, hence the values of j used for the substituted ansatz are j = p, s, i. DC-3WM can be considered as a specialisation of NP-4WM, where the DC tone is represented by one of the pump tones having a frequency of 0 and can be achieved by making the transformations: $\omega_{p_2} \to 0$, $\gamma_{p_2} \to 0$, $\omega_{p_1} \to \omega_p$, $\gamma_{p_1} \to \gamma_p$, $A_{p_1} \to A_p$, and $A_{p_2} = A_{p_2}^* \to I_{DC}$, it can be shown that CMEs in (8a)-(8d) reduce to,

$$\frac{dA_p}{dz} = \frac{\beta_p^2}{8\gamma_p I_*^2}[(e^{-(\gamma_p+\gamma_p^*)z}\,|A_p|^2 + 2e^{-(\gamma_s+\gamma_s^*)z}\,|A_s|^2 + 2e^{-(\gamma_i+\gamma_i^*)z}\,|A_i|^2 + 2I_{DC}^2)A_p + 2e^{(\gamma_p-\gamma_s-\gamma_i)z}A_iA_sI_{DC}] \tag{2.1a}$$

$$\frac{dA_s}{dz} = \frac{\beta_s^2}{8\gamma_s I_*^2}[(e^{-(\gamma_s+\gamma_s^*)z}\,|A_s|^2 + 2e^{-(\gamma_i+\gamma_i^*)z}\,|A_i|^2 + 2e^{-(\gamma_p+\gamma_p^*)z}\,|A_p|^2 + 2I_{DC}^2)A_s + 2e^{(\gamma_s-\gamma_i^*-2\gamma_p)z}A_i^*A_pI_{DC}] \tag{2.1b}$$

$$\frac{dA_i}{dz} = \frac{\beta_i^2}{8\gamma_i I_*^2}[(e^{-(\gamma_i+\gamma_i^*)z}\,|A_i|^2 + 2e^{-(\gamma_p+\gamma_p^*)z}\,|A_p|^2 + 2e^{-(\gamma_s+\gamma_s^*)z}\,|A_s|^2 + 2I_{DC}^2)A_i + 2e^{(\gamma_i-\gamma_s^*-2\gamma_p)z}A_s^*A_pI_{DC}], \tag{2.1c}$$

with (8b) reducing to the trivial $\frac{dI_{DC}}{dz} = 0$. These are the lossy CMEs for DC-3WM. For completeness, the CMEs for the lossless DC-3WM regime are given by,

$$\frac{dA_p}{dz} = -\frac{i\beta_p}{8I_*^2}[(|A_p|^2 + 2\,|A_s|^2 + 2\,|A_i|^2 + 2I_{DC})A_p + 2A_iA_sI_{DC}e^{-i\Delta_\beta^{(D3)}z}] \tag{2.2a}$$

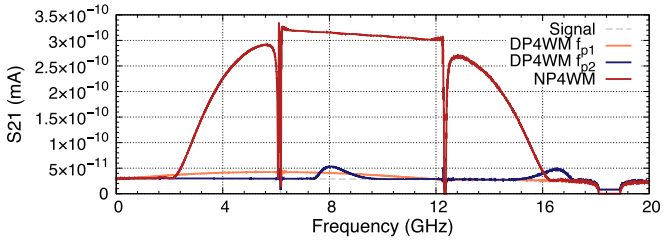

Figure C1. Transmission comparison between NP-4WM, and DP-4WM regimes for 6-12 GHz KITWPA.

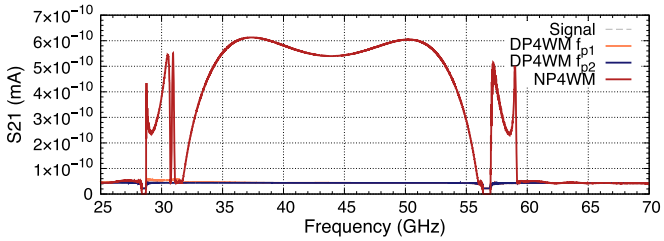

Figure C2. Transmission comparison between NP-4WM, and DP-4WM regimes for ALMA Band-1 KITWPA.

$$\frac{dA_s}{dz} = -\frac{i\beta_s}{8I_*^2}[(|A_s|^2 + 2\,|A_i|^2 + 2\,|A_p|^2 + 2I_{DC})A_s + 2A_i^* A_p I_{DC} e^{i\Delta_\beta^{(D3)} z}] \quad (2.2b)$$

$$\frac{dA_i}{dz} = -\frac{i\beta_i^2}{8I_*^2}[(|A_i|^2 + 2\,|A_p|^2 + 2\,|A_s|^2 + 2I_{DC})A_i + 2A_s^* A_p I_{DC} e^{i\Delta_\beta^{(D3)} z}], \quad (2.2c)$$

where $\Delta_\beta^{(3)} = \beta_s + \beta_i - \beta_p$.

Appendix C. Analysis of parasitic DP-4WM modes

The simulations presented in this paper assume that the only wave mixing process taking place is the NP-4WM process, with the relation given by $f_i^{(NP-4WM)} = f_{p_1} + f_{p_2} - f_s$, although there could also be other DP-4WM processes taking place, such as those described by $f_i^{(DP-4WM),\,1} = 2f_{p_1} - f_s$ and $f_i^{(DP-4WM),\,2} = 2f_{p_2} - f_s$. In general, the phase matching condition for these DP-4WM modes will be different to that of the NP-4WM mode, hence it is assumed they will be suppressed when a KITWPA is operating in the NP-4WM. To investigate the validity of this assumption we have simulated the performance of these parasitic DP-4WM modes relative to the NP-4WM mode for some of the KITWPA designs discussed in the main body of this article.

Figure C1 compares the strength of the various wave mixing modes for the 6-12 GHz KITWPA design by plotting the output amplitudes for the signal tone produced for each mode. This plot clearly shows that whilst the amplitudes for the parasitic DP-4WM modes are are non-zero, they are significantly weaker than the NP-4WM mode, since they are suppressed due to being phase mismatched, hence they have a negligible effect on the gain profile of a KITWPA operating in a NP-4WM mode.

Figure C2 plots the same values as shown in figure C1, except this time for the ALMA Band-1 KITWPA. As discussed in section 4.1, this KITWPA design utilises the curvature of the dispersion relation, rather than the periodic stopbands to suppress the higher harmonics of the pump tones. We can see from figure C2, however, that we observe very similar behaviour to that shown in figure C1, i.e., we observe that the parasitic DP-4WM modes are suppressed and have very little effect on the NP-4WM gain profile.

The plots presented in this section, therefore, justify the assumption that the NP-4WM mode is the only wave mixing process efficiently taking place along the KITWPA devices in this paper, hence the CMEs presented in (8a)-(8d) provide a good prediction of the real gain performance of a NP-4WM KITWPA device.

ORCID iDs

J C Longden https://orcid.org/0009-0005-9519-2547
B-K Tan https://orcid.org/0000-0002-6252-9351

References

[1] Noroozian O 2020 *Cycle 5 NRAO ALMA Development Study Report Technology Development of Quantum-Limited , Ultra-Wideband RF Amplifiers for ALMA : A 65-150 GHz Test Case*
[2] Zobrist N *et al* 2019 Wide-band parametric amplifier readout and resolution of optical microwave kinetic inductance detectors *Appl. Phys. Lett.* **115** 042601
[3] Che G *et al* 2017 A Superconducting Phase Shifter and Traveling Wave Kinetic Inductance Parametric Amplifier for W-Band Astronomy 1710.11335
[4] Backes K M *et al* 2021 A quantum enhanced search for dark matter axions *Nature* **590** 238–42
[5] Kutlu C ,, Van Loo A, Uchaikin S, Matlashov A, Lee D, Oh S, Kim J, Chung W, Nakamura Y and Semertzidis Y 2021 Characterization of a flux-driven Josephson parametric amplifier with near quantum-limited added noise for axion search experiments *Superconductor Science and Technology* **34** 1–7
[6] Braine T *et al* 2020 Extended Search for the Invisible Axion with the Axion Dark Matter Experiment *Phys. Rev. Lett.* **124** 101303
[7] Arute F *et al* 2019 Quantum supremacy using a programmable superconducting processor *Nature* **574** 505–10
[8] Lecocq F, Quinlan F, Cicak K, Aumentado J, Diddams S A and Teufel J D 2021 Control and readout of a superconducting qubit using a photonic link *Nature* **591** 575–9
[9] Gonzalez-Zalba M F, de Franceschi S, Charbon E, Meunier T, Vinet M and Dzurak A S 2021 Scaling silicon-based quantum computing using CMOS technology *Nat Electron* **4** 872–84
[10] Eom B H, Day P, Leduc H G and Zmuidzinas J 2012 A wideband, low-noise superconducting amplifier with high dynamic range *Nat. Phys.* **8** 623–7
[11] Bockstiegel C, Gao J, Vissers M R, Sandberg M, Chaudhuri S, Sanders A, Vale L R, Irwin K D and Pappas D P 2014 Development of a broadband NbTiN traveling wave parametric amplifier for MKID readout *J. Low Temp. Phys.* **176** 476–82 Springer New York LLC
[12] Vissers M R, Erickson R P, Ku H S, Vale L, Wu X, Hilton G C and Pappas D P 2016 Low-noise kinetic inductance traveling-wave amplifier using three-wave mixing *Appl. Phys. Lett.* **108** 1–5
[13] Goldstein S, Kirsh N, Svetitsky E, Zamir Y, Hachmo O, De Oliveira C E and Katz N 2020 Four wave-mixing in a microstrip kinetic inductance travelling wave parametric amplifier *Appl. Phys. Lett.* **116** 1–4
[14] Shu S, Klimovich N, Eom B H, Beyer A D, Basu Thakur R, Leduc H G and Day P K 2021 Nonlinearity and wide-band parametric amplification in a (Nb,Ti)N microstrip transmission line *Physical Review Research* **3** 1–9
[15] Klimovich N, Day P, Shu S, Eom B H, Leduc H and Beyer A 2023 Demonstration of a quantum noise limited traveling-wave parametric amplifier 2306.11028
[16] Longden J C, Boussaha F M and Chaumont C 2021 Kitti Ratter, and Boon-Kok Tan. Preliminary characterisation of titanium nitride thin film at 300 mK for the development of kinetic inductance travelling wave parametric amplifiers *Quantum Technology: Driving Commercialisation of an Enabling Science II* **1188113** 38
[17] Kow C, Podolskiy V and Kamal A 2022 Self phase-matched broadband amplification with a left-handed Josephson transmission line. 2201.04660
[18] Qiu J Y *et al* 2023 Broadband squeezed microwaves and amplification with a Josephson travelling-wave parametric amplifier *Nat. Phys.* **19** 706–13
[19] Inoue K 1992 Four-wave mixing in an optical fiber in the zero-dispersion wavelength region *J. Lightwave Technol.* **10** 1553–61
[20] Aso O, Tadakuma M and Namiki S 2000 Four-wave mixing in optical fibers and its applications *Furukawa Rev.* **19** 63–8
[21] Ho Eom B, Day P K, Leduc H G and Zmuidzinas J 2012 A wideband, low-noise superconducting amplifier with high dynamic range *Nat. Phys.* **8** 623–7
[22] Pozar D M 2012 *Pozar. Microwave Engineering* (New York: Wiley) 4th edn
[23] Chaudhuri S 2013 Measurement, Simulation, and Design of the Dispersion-Engineered Traveling-Wave Kinetic Inductance Amplifier *PhD thesis* California Institute of Technology
[24] Tan B-K, Boussaha F, Chaumont C, Longden J C and Montilla J N 2022 Engineering the thin film characteristics for optimal performance of superconducting kinetic inductance amplifiers using a rigorous modelling technique *Open Research Europe* **2** 88
[25] Shan W, Sekimoto Y and Noguchi T 2016 Parametric Amplification in a Superconducting Microstrip Transmission Line *IEEE Trans. Appl. Supercond.* **26** 1–9
[26] Chaudhuri S, Li D, Irwin K D, Bockstiegel C, Hubmayr J, Ullom J N, Vissers M R and Gao J 2017 Broadband parametric amplifiers based on nonlinear kinetic inductance artificial transmission lines *Appl. Phys. Lett.* **110** 152601
[27] Malnou M, Vissers M R, Wheeler J D, Aumentado J, Hubmayr J, Ullom J N and Gao J 2021 A three-wave mixing kinetic inductance traveling-wave amplifier with near-quantum-limited noise performance *PRX Quantum* **2** 010302
[28] Tan B-K, Klimovich N, Stephenson R, Faramarzi F and Day P 2024 Operation of Kinetic-Inductance Travelling Wave Parametric Amplifiers at Millimetre Wavelengths *Superconductor Science and Technology* (https://doi.org/10.1088/1361-6668/ad20fd)
[29] ALMA Receiver Bands | ESO 26 Jan 2024 (https://eso.org/public/teles-instr/alma/receiver-bands/)
[30] Zhao S, Goldie D J and Thomas C N 2019 Loss and saturation in superconducting travelling-wave parametric amplifiers *J. Phys. D: Appl. Phys.* **52** 1–8